The Astrophysical Journal, 845:172 (13pp), 2017 August 20 https://doi.org/10.3847/1538-4357/aa8220

Discovery of a Protocluster Associated with a Lyα Blob Pair at $z = 2.3$

Toma Bădescu[1], Yujin Yang[1,2], Frank Bertoldi[1], Ann Zabludoff[3], Alexander Karim[1], and Benjamin Magnelli[1]
[1] Argelander Institut für Astronomie, Universität Bonn, Auf dem Hügel 71, D-53121 Bonn, Germany; toma@astro.uni-bonn.de
[2] Korea Astronomy and Space Science Institute, 776 Daedeokdae-ro, Yuseong-gu, Daejeon 34055, Korea
[3] Steward Observatory, University of Arizona, 933 North Cherry Avenue, Tucson, AZ 85721, USA
Received 2017 May 2; revised 2017 July 10; accepted 2017 July 20; published 2017 August 23

Abstract

Bright Lyα blobs (LABs)—extended nebulae with sizes of $\sim$100 kpc and Lyα luminosities of $\sim 10^{44}$ erg s^{-1}—often reside in overdensities of compact Lyα emitters (LAEs) that may be galaxy protoclusters. The number density, variance, and internal kinematics of LABs suggest that they themselves trace group-like halos. Here, we test this hierarchical picture, presenting deep, wide-field Lyα narrowband imaging of a $1^\circ \times 0.^\circ5$ region around a LAB pair at $z = 2.3$ discovered previously by a blind survey. We find 183 Lyα emitters, including the original LAB pair and three new LABs with Lyα luminosities of (0.9–1.3) $\times$ 10^{43} erg s^{-1} and isophotal areas of 16–24 arcsec^2. Using the LAEs as tracers and a new kernel density estimation method, we discover a large-scale overdensity (Boötes J1430+3522) with a surface density contrast of $\delta_\Sigma = 2.7$, a volume density contrast of $\delta \sim 10.4$, and a projected diameter of $\approx$20 comoving Mpc. Comparing with cosmological simulations, we conclude that this LAE overdensity will evolve into a present-day Coma-like cluster with $\log(M/M_\odot) \sim 15.1 \pm 0.2$. In this and three other wide-field LAE surveys re-analyzed here, the extents and peak amplitudes of the largest LAE overdensities are similar, not increasing with survey size, and implying that they were indeed the largest structures then and today evolve into rich clusters. Intriguingly, LABs favor the outskirts of the densest LAE concentrations, i.e., intermediate LAE overdensities of $\delta_\Sigma = 1$–2. We speculate that these LABs mark infalling protogroups being accreted by the more massive protocluster.

Key words: galaxies: clusters: general – galaxies: formation – galaxies: high-redshift – intergalactic medium – large-scale structure of universe

Supporting material: machine-readable tables

1. Introduction

The study of galaxy clusters plays an important role in understanding cosmological structure formation and the astrophysics of galaxy evolution. Statistics of galaxy cluster size, mass, and redshift distribution provide constraints for cosmological models, while the properties of the galaxies and gas inside clusters give clues about galaxy evolution and the star formation history of the universe (Press & Schechter 1974; Lanzetta et al. 1995; Lilly et al. 1996; Madau et al. 1998; Boylan-Kolchin et al. 2009). The progenitors of galaxy clusters, the so-called protoclusters, start off as overdense regions and groups of galaxies at high redshift, which over time coalesce into the larger galaxy clusters we see today. While galaxy clusters at $z < 1$ are routinely discovered by various techniques such as the red sequence of galaxies (e.g., Gladders & Yee 2000, 2005), the X-ray emission from hot intracluster gas (Rosati et al. 2002; Mullis et al. 2005; Stanford et al. 2006), or the Sunyaev Zel'dovich effect on CMB photons (Zeldovich et al. 1972; Bleem et al. 2015), observing the early stages of cluster formation at higher redshifts has been challenging.

Since protoclusters lack many of the observational properties of the massive virialized galaxy clusters of today, one of the best ways to find them is to identify galaxy overdensities at high redshift (Overzier 2016). Readily observable populations of galaxies include radio galaxies (Venemans et al. 2002, 2007; Hatch et al. 2011a; Hayashi et al. 2012; Wylezalek et al. 2013; Cooke et al. 2014), submillimeter galaxies (Daddi et al. 2009; Capak et al. 2011; Dannerbauer et al. 2014; Rigby et al. 2014), hydrogen alpha emitters (Hatch et al. 2011b; Hayashi et al. 2012), or Lyman break galaxies, and Lyman alpha emitters (LAEs) (e.g., Taniguchi et al. 2005; Overzier et al. 2006, 2008). LAEs, which are compact galaxies that have strong emission in the Lyα line, are relatively easy to observe over a wide range of redshifts at $z \sim$ 2–6 (e.g., Taniguchi et al. 2005; Gronwall et al. 2007; Nilsson et al. 2009; Guaita et al. 2010). LAEs are mainly star-forming, low-mass objects, and some may be the progenitors of today's Milky Way-type galaxies (Gawiser et al. 2007). With wide-field, deep narrowband surveys centered on the Lyα line emission at a given redshift, one can use LAEs to identify galaxy overdensities. Giant Lyα-emitting nebulae, also known as Lyα "blobs" (LABs; Francis et al. 1996; Ivison et al. 1998; Steidel et al. 2000; Matsuda et al. 2004; Palunas et al. 2004), which emit Lyα radiation on large scales (50–100 kpc) and have high Lyα luminosities of 10^{43-44} erg s^{-1}, are also apparent tracers of LAE overdensities (e.g., Matsuda et al. 2004, 2005; Saito et al. 2006; Prescott et al. 2008; Yang et al. 2009, 2010).

What powers the strong extended Lyα emission in blobs is still poorly understood. Possible powering mechanisms include gravitational cooling radiation (Haiman et al. 2000; Fardal et al. 2001; Yang et al. 2006; Dijkstra & Loeb 2009; Faucher-Giguère et al. 2010; Goerdt et al. 2010; Rosdahl & Blaizot 2012), the resonant scattering of Lyα photons produced by star formation (Møller & Warren 1998; Laursen & Sommer-Larsen 2007; Hayes et al. 2011; Steidel et al. 2011; Zheng et al. 2011; Cen & Zheng 2013), and photoionizing radiation from active galactic nuclei (AGNs) (Haiman & Rees 2001; Cantalupo et al. 2005; Geach et al. 2009; Kollmeier et al. 2010; Overzier et al. 2013; Yang et al. 2014a). Another potential source is shock-heating from starburst-driven winds (Taniguchi & Shioya 2000; Mori & Umemura 2006), although recent

studies of the emission of non-resonant lines from eight Lyα blobs exclude models that require fast galactic winds driven by AGNs or supernovae (Yang et al. 2011, 2014a, 2014b; Prescott et al. 2015a).

Regardless of the energy sources of Lyα blobs, the association of blobs with compact LAE overdensities with sizes of $\sim$10–20 Mpc (Matsuda et al. 2004, 2011; Palunas et al. 2004; Yang et al. 2010; Prescott et al. 2012, 2008; Saito et al. 2015), suggests that LABs are good potential markers of large protoclusters. Furthermore, the number density and variance of Lyα blobs, as well as the 200–400 km s^{-1} relative velocities of their embedded galaxies, suggest that blobs themselves occupy individual group-like halos of $\sim 10^{13}\,M_{\odot}$ (Yang et al. 2010, 2011; Prescott et al. 2012, 2015b). Thus, blobs may be sites of massive galaxy formation and trace significant components of the build-up of protoclusters. However, because most previous LAB studies have been carried out toward known overdense regions or protoclusters, the observed relationship between Lyα blobs and LAE overdensities may be biased. To probe the LAB-overdensity connection one should investigate the area around known Lyα blobs that were identified without prior knowledge of their environments. For example, Prescott et al. (2008) studied the environment of a Lyα blob that was serendipitously discovered by its strong Spitzer MIPS 24 μm flux (Dey et al. 2005), finding that this Lyα blob resides in an overdense region of 20×50 Mpc^2.

In this work, we investigate the large-scale environment of a Lyα blob pair at redshift $z = 2.3$ that was discovered without prior knowledge of the environment (Yang et al. 2009). The paper is organized as follows. In Section 2, we present our observations and data reduction. In Section 3, we discuss our selection of Lyα emitters and blobs. In Section 4, we describe the discovery of an overdensity associated with the Lyα blob pair, compare its properties with those obtained from three previous narrowband surveys of other LAE structures, discuss whether it will evolve into a present-day galaxy cluster, and show that Lyα blobs are preferentially located in the outskirts of protoclusters here and in the other surveys. In Section 5, we summarize the results. Throughout the paper, we adopt the following cosmological parameters: $H_0 = 70$ km s^{-1} Mpc^{-1}, $\Omega_{\rm M} = 0.3$, and $\Omega_{\Lambda} = 0.7$. All distances presented are in the comoving scale unless noted otherwise, and all magnitudes are in the AB system (Oke 1974).

2. Observations and Data Reduction

Yang et al. (2009) conducted a wide-field narrowband survey covering an area of 4.82 deg^2 of the Boötes NDWFS, targeting Lyα emission at $z = 2.3$, and obtained an unbiased sample of the largest and brightest Lyα blobs at that redshift. The redshift was chosen to facilitate future observations of the extended Lyα gas via the optically thin Hα 6563 Åline, which is redshifted into a relatively sky-line-free part of the infrared spectrum. Yang et al. (2009) discovered four Lyα blobs with luminosities of 1.6–5.3 $\times$ 10^{43} erg s^{-1} and isophotal areas 28–57 arcsec^2. Two of the four blobs form a pair, with a separation of only 70″ (550 kpc at $z = 2.3$), which makes them ideal targets for our deeper follow-up Lyα survey to map the spatial distribution of LAEs and LABs described here.

We obtain narrowband images covering a total area of $\sim 1^{\circ} \times 0.^{\circ}5$ around the two known Lyα blobs (Yang et al. 2009) using the Mosaic1.1 camera on the Kitt Peak National Observatory (KPNO) Mayall 4 m telescope. In Figure 1 we show the areas covered by the National Optical Astronomical Observatory (NOAO) Deep Wide-field Survey (NDWFS) and the locations of our two pointings (hereafter Boötes1 and Boötes2) centered on $14^{\rm h}31^{\rm m}42.^{\rm s}22$, $+35^{\circ}31'19.''9$ and $14^{\rm h}28^{\rm m}54.^{\rm s}08$, $+35^{\circ}31'19.''9$. Observations were carried out on 2011 April 29 and 30, with exposure times of 7.3 and 6.0 hr, respectively. During the two observing nights, the average seeing was $\approx 1.''1$.

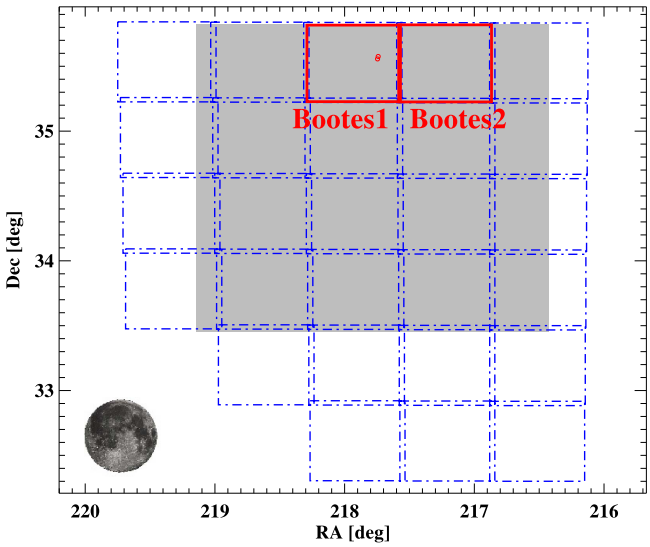

Figure 1. The extents of the NOAO Deep Wide-field Survey and the previous Lyα narrowband imaging survey (Yang et al. 2009) are shown in blue rectangles and the shaded region in gray, respectively. The two fields that we targeted in this work are indicated in red. The Lyα blob pair discovered by Yang et al. (2009) is marked with red circles. The total field of view of our new imaging has dimensions of $69.'5 \times 35.'6$ or 112.9 Mpc $\times$ 57.9 Mpc, with a line-of-sight depth of $\approx$46.4 Mpc. The Moon is shown for scale.

We observe with the custom narrowband filter used in the discovery of the known Lyα blob pair (Yang et al. 2009). The filter has a central wavelength of $\lambda_c = 4030$ Å and a bandwidth of $\Delta\lambda_{\rm FWHM} = 47$ Å, corresponding to the Lyα emission at $z = 2.3$ and a line-of-sight depth of $\approx$46.4 Mpc ($\Delta z = 0.0037$). Apart from the narrowband (NB) images, we also use NDWFS broadband B_W-, R-, and I-band images for continuum estimation.

We reduce the data using the `MSCRED` package in `IRAF` (Tody 1986). We correct the images for cross-talk and bias, then apply the flat-field correction, using both dome and sky-flats. Bad pixels and satellite trails are masked, and cosmic rays are removed using the `LA-COSMIC` software (van Dokkum 2001). We flux-calibrate by observing 3–4 spectrophotometric standard stars per night, with typical uncertainties in flux calibration of $\sim$0.02–0.04 mag. The astrometry of our images is improved with the `msccmatch` tasks in `IRAF` using the USNO-B1.0 (Monet et al. 2003) catalog. After matching the image scales, we stack them using the `mscstack` task. The total field of view has dimensions of $69.'5 \times 35.'6$ or 112.9 Mpc $\times$ 57.9 Mpc, with a total survey volume of 3.03 $\times 10^5$ Mpc^3.

3. Analysis

3.1. Selection of Lyα Emitters

We run Source Extractor (`SExtractor`; Bertin & Arnouts 1996) on the NB image and select sources having at least four adjacent pixels above the 1σ local background rms,

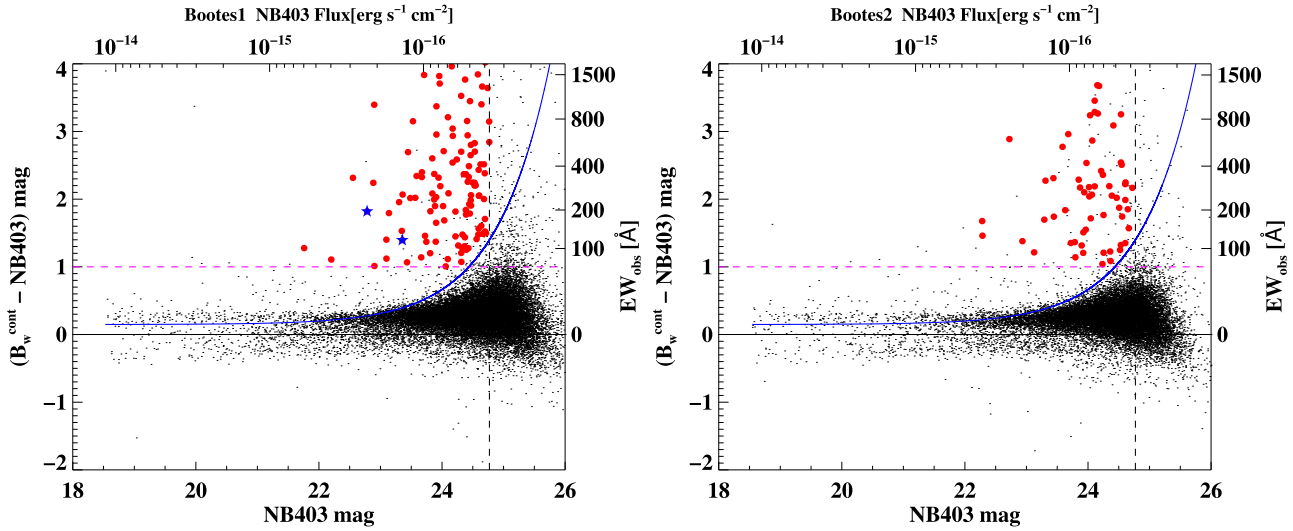

Figure 2. Color–magnitude plots of objects in the Boötes1 (left) and Boötes2 (right) fields (black dots). Lyα-emitter candidates are marked with red dots. The blue stars represent the two known blobs from Yang et al. (2009). The horizontal dashed line marks the cut in $EW_{obs} > 67$ Å, while the vertical one represents the cut in NB magnitude at 24.77. The blue curve represents the 5σ NB magnitude error cut.

identifying ∼45,000 sources. After applying a 3 × 3 pixel (0.768 × 0.768 arcsec) boxcar filter to the NB and B_W images, we extract the NB and B_W magnitudes inside circular 3″ apertures centered on the selected sources. From these we determine the Lyα line flux, equivalent width (EW), and underlying continuum flux for each of our objects using the following relations:

$$f^{\lambda}_{\rm cont} = \frac{F_{Bw} - F_{\rm NB}}{\Delta\lambda_{Bw} - \Delta\lambda_{\rm NB}}, \quad (1)$$

$$F_{\rm line} = F_{\rm NB} - \Delta\lambda_{\rm NB} \cdot f^{\lambda}_{\rm cont}, \quad (2)$$

$$B_W^{\rm cont} = -2.5\log\left(f^{\lambda}_{\rm cont}\frac{\lambda^2_{\rm NB}}{c}\right) - 48.6, \quad (3)$$

where $f^{\lambda}_{\rm cont}$ is the continuum flux density, $F_{\rm line}$ is the Lyα line flux, $F_{\rm NB}$ and F_{Bw} are the fluxes in the NB and B_W bands, respectively, and $\Delta\lambda_{\rm NB}$, $\Delta\lambda_{Bw}$ are the bandwidths of the two filters. $B_W^{\rm cont}$ is the AB continuum magnitude, without the line contribution, and $\lambda_{\rm NB} = 4030$ Å is the central wavelength of the NB filter.

To identify excess Lyα emission, we calculate the color index ($B_W^{\rm cont}$ − NB) of all our candidate sources. We create the Lyα emitter sample by applying the following selection criteria to the extracted objects:

1. $B_W^{\rm cont} - {\rm NB} \geqslant 1$, corresponding to $EW_{\rm obs} \geqslant 67$Å
2. NB $\leqslant 24.77$(5.5σ detection threshold)
3. $B_W^{\rm cont} - {\rm NB} \geqslant 5\sigma_{\rm NB}$,

where $B_W^{\rm cont}$ is the continuum magnitude of an object, without the Lyα line emission. The 5.5σ narrowband detection threshold corresponds to a Lyα luminosity of 1.6×10^{42} erg s^{-1}, which is ≈3 times deeper than the original wide-field survey (Yang et al. 2009).

In Figure 2, we show the NB magnitude versus color index and EW for the Boötes 1 and Boötes 2 fields. The dashed vertical and horizontal lines correspond to our selection criteria in NB magnitude and color, respectively. After applying these cuts, we are left with a sample of 354 objects. The blue solid lines correspond to the cut-imposed requirement that the color index should be larger than 5 times the error in the NB magnitude, which eliminates 77 objects from our sample. Removing objects that are close to bright stars or less than 50 pixels away from the image edges further reduces the size of the sample to 223 objects. Finally, we inspect the sample visually, eliminating obvious false detections, like bright nearby galaxies or image artifacts, producing a final sample of 183 objects. We consider sample contamination from [O II] λ3727 emission in galaxies at $z \approx 0.08$. The rest-frame EW of [O II] emitters at $z = 0.1$–0.2 is <50 Å (Hogg et al. 1998; Ciardullo et al. 2013), below our EW cut. Given that [O II] EWs e-fold with a scale length of 6 Å–14 Å (Ciardullo et al. 2013), we estimate that the probability of finding [O II] interlopers with $EW_{\rm obs} > 67$ Å is less than 1%. We list the properties of the 183 Lyα emitters in Table 1.

We test how our selection criteria might influence the size and spatial distribution of our LAE sample. We create 81 different Lyα-emitter samples by varying the selection criteria around our original values. We vary the color index cuts, from 0.8 to 1.2, in nine steps of 0.05, and the NB magnitude cuts, from 24.69 to 24.85, in nine steps of 0.02 mag. Comparing all the resulting samples to the one we originally adopted for this work, we find that the influence of using these different selection criteria on the large-scale distribution of objects is minimal (see Section 4.1).

3.2. Selection of Lyα Blobs

With deeper NB imaging data than those in Yang et al. (2009), we search for Lyα blobs with intermediate luminosities and sizes that our prior shallower survey might have missed. Using Equations (1) and (2), we calculate the Lyα line flux for each pixel. The 1σ surface brightness limit of the resulting Lyα line image is $\sim 2.1 \times 10^{-18}$ erg s^{-1} cm^{-2} arcsec^{-2} per 1 arcsec^2 aperture, which makes this survey 1.5–2.2 times deeper than the original wide-field survey that led to our discovery of the LAB pair (Yang et al. 2009). We run `SExtractor` on the line image, selecting sources with at least 16 adjacent pixels above the 5σ surface brightness limit. Then, we cross-match this catalog with our emitter sample above to make sure that the extracted Lyα blob candidates do have a Lyα line excess. We select Lyα blob

Table 1
Catalog of Lyα-emitter Candidates

ID	R.A. (J2000)	Decl. (J2000)	$\log(L_{Ly\alpha})$	EW (Å)
1	14:32:36.39	+35:23:34.7	42.41 ± 0.05	83
2	14:32:13.86	+35:14:29.3	42.52 ± 0.04	113
3	14:30:27.02	+35:14:32.7	42.17 ± 0.08	314
4	14:32:08.58	+35:14:37.6	41.63 ± 0.25	137

(This table is available in its entirety in machine-readable form.)

candidates by requiring that their isophotal area above the surface Lyα brightness threshold of 4.45×10^{-18} erg s^{-1} cm^{-2} arcsec^{-2} is larger than 16 arcsec^2 . We initially find seven objects matching this criterion, including the two known blobs. In order to estimate possible sample contamination, we place artificial point sources having $L(\mathrm{Ly}\alpha) = 10^{41-44}$ erg s^{-1} in our Lyα images and extract them using the same procedures as for the LABs.

Because the noise and background level of the image can vary across the field, we also test how reliably we can recover extended Lyα emission for the LAB candidates. We cut out 101×101 pixels regions around the candidates from the Lyα line image, centered on the candidates, and place them in 4000 empty sky regions in the Boötes 1 and 2 fields. We then run the source extraction procedure using the same settings used for the real data. The measured size and luminosities of the Lyα blob candidates will vary depending on the position in the field. The variance of the source properties recovered this way gives us the uncertainties on the luminosities and sizes of the candidates introduced by placing the objects in different parts of the field. The recovery fraction is defined as the fraction of times the Lyα blob candidate is recovered with a size above 16 arcsec^2 . Out of the seven initial candidates, five candidates—including the already known blob pair—have recovery fractions higher than 90%. We consider these to be our LAB sample. The 90% recovery threshold was chosen because the rest of the recovered blobs have much lower recovery fractions: two blobs with 75% and the rest well below the 50% recovery fraction. In Figure 3, we show the isophotal area of the Lyα blob candidates against their Lyα luminosity, as well as the relations for the simulated point sources. The Lyα blob candidates are located at higher isophotal areas for a given luminosity, clearly separated from the locus of point sources.

In Figure 4, we show all our Lyα blob candidates, including the two known Lyα blobs of Yang et al. (2009), in the NB, Lyα line, B_W-, R-, and I-bands, respectively. The shapes of the Lyα blob candidates are irregular and their isophotal areas exceed those of their continuum counterparts. In Table 2, we list the properties of the three new Lyα blobs, including position, luminosity, and size. Their Lyα luminosities lie in the range of $(0.9\text{–}1.4) \times 10^{43}$ erg s^{-1}.

4. Results and Discussion

4.1. Discovery of a LAE-traced Protocluster Associated with LABs

Using our 183 Lyα emitter and blob sample, we investigate the large-scale environment around the known Lyα blob pair (Yang et al. 2009). In Figure 5(a), we show the spatial distribution of our Lyα emitters—which includes the new Lyα blobs—across the $69\farcm3 \times 35\farcm4$ field. We mark the locations of our 183 Lyα emitters, and indicate the areas that were excluded from our analysis because of contamination from bright sources such as stars.

To estimate the smooth surface density distribution from the discrete positions of the detected galaxies, one often convolves the position map with a Gaussian kernel of width σ. The width of this kernel affects the resulting surface density distribution, yet there is no single way of selecting the smoothing method and size of a smoothing kernel. The kernel size is often chosen to match the mode (Saito et al. 2015) or the median (Matsuda et al. 2011) of the distances between objects in a sample. Matsuda et al. (2005) selected a kernel width that matched the redshift dispersion introduced by the peculiar velocity dispersion of their LAE sample, and Yang et al. (2010) used an adaptive kernel technique to smooth their LAE sample. In this paper, we choose a different approach, one meant to find the kernel size generating the smoothed density field that has the highest probability of representing our LAE sample. This technique is described in detail in the Appendix, and we briefly explain it here.

Assuming our LAEs' positions are randomly drawn from an unknown underlying density distribution f, we use kernel density estimation (KDE) to find an estimate $\hat{f}$ for the density distribution function. Our method involves convolving the discrete object map with Gaussian kernels, thus generating smooth density maps. Each map is generated using a different kernel width σ. We search for the σ value that maximizes the likelihood to observe our Lyα-emitter sample, given the density distribution estimate $\hat{f}$. We find this optimum value for the kernel width to be $\sigma = 2\farcm63$, which is used for the smoothed image in Figure 5(b).

The Lyα-emitter density map in Figure 5(b) reveals a significant overdensity near the field center (R.A. = $14^{\mathrm{h}}30^{\mathrm{m}}35\overset{\mathrm{s}}{.}7$, decl. = $+35°22'06\farcs2$), with a projected radius of ∼10 Mpc. This overdense region is in both Boötes1 and 2 image frames, and thus is unlikely to be caused by different observing conditions for the two fields or different sample-selection criteria.

To test if the surface density maps change due to the different selection criteria, we create 81 surface density maps, eachcorresponding to a different cut in color index and NB magnitude as described in Section 3.1. Figure 5(c) shows the mean and variance of the Lyα-emitter surface density of these 81 maps. The average density map shows an overdensity that is very similar in size and position to the one we obtained using our selection criteria. The variance is largest away from the overdense region, indicating that the overall number density and density contrast of the overdense region is not strongly dependent on the LAE selection criteria.

To illustrate the size of the overdense region, we show the radial distribution of Lyα emitters in Figure 6. The Lyα-emitter surface density peaks at $\Sigma_{\mathrm{overdense}} \sim 0.27$ arcmin^{-2} Δz^{-1} inside a ∼8 Mpc (5′) radius centered on the overdense region, decreasing to $\Sigma_{\mathrm{field}} = (5.4 \pm 0.9) \times 10^{-2}$ arcmin^{-2} Δz^{-1} at radii larger than 25 Mpc, with an average value of $\bar{\Sigma} = (7.4 \pm 0.54) \times 10^{-2}$ arcmin^{-2} Δz^{-1} over the entire survey. The scale of this structure clearly demonstrates that one needs a very wide-field survey over ∼100 Mpc to reliably measure the overdensity relative to the background field region.

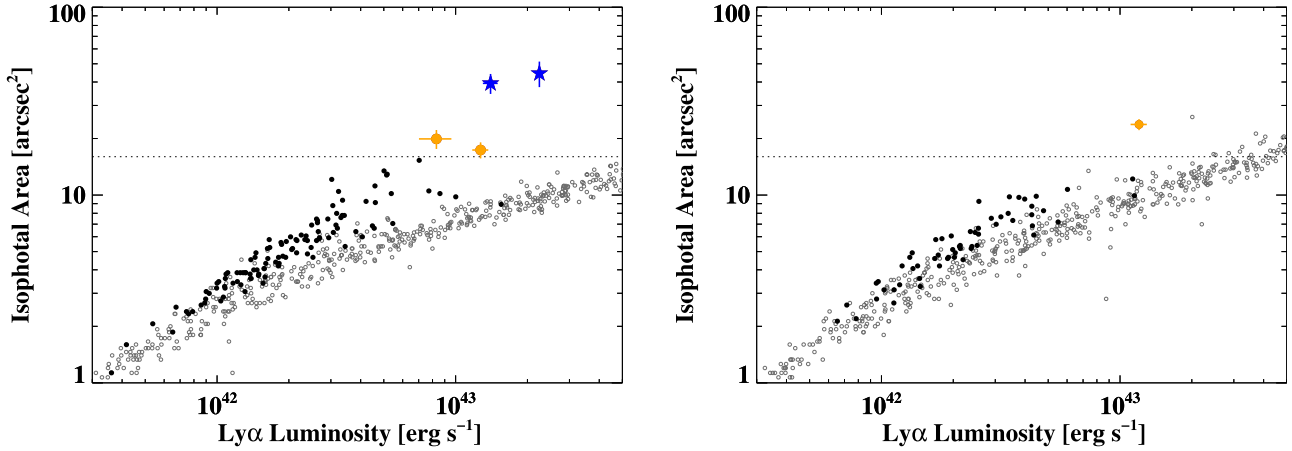

Figure 3. Lyα luminosity vs. the isophotal area of Lyα emitters, including Lyα blobs, for the Boötes1 field (left) and the Boötes2 field (right). Lyα emitters, the three new Lyα blob candidates, and the two known blobs (Yang et al. 2009) are shown as black dots, filled orange circles, and blue stars, respectively. The dotted horizontal line marks the selection criteria for our Lyα blobs: an isophotal area greater than 16 arcsec^2 above the 4.45×10^{-18} erg s^{-1} cm^{-2} arcsec^{-2} brightness limit. The gray circles represent simulated point sources in our fields.

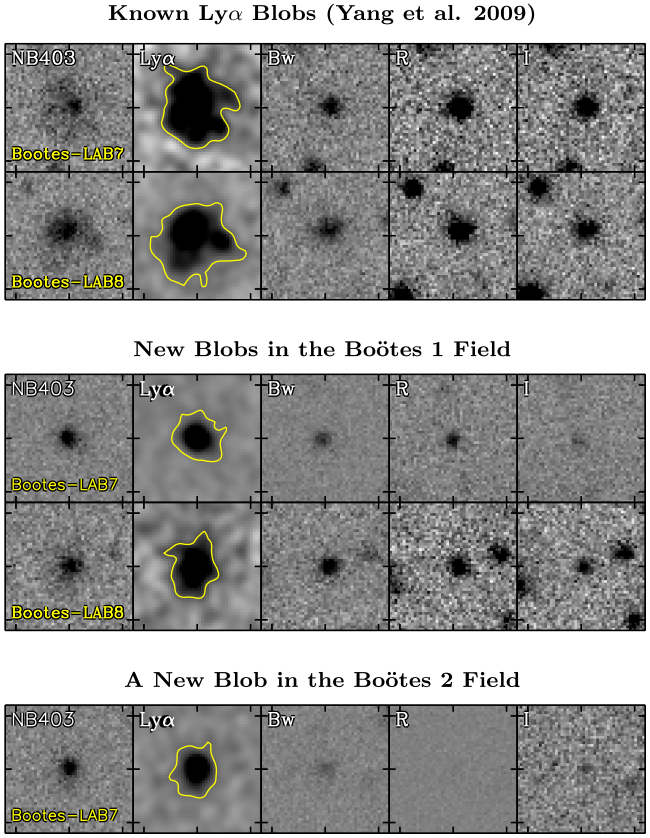

Figure 4. Images of the three new Lyα blob candidates (bottom three rows) and of the two known blobs from Yang et al. (2009) (top two rows). From left to right: NB, continuum-subtracted Lyα image, B_w-, R-, and I-bands, respectively. The contours represent the surface brightness of 4.45×10^{-18} erg s^{-1} cm^{-2} arcsec^{-2}. The isophotal areas of the new intermediate blobs are $\approx$16 arcsec^2, with luminosities of (0.9–1.4) $\times$ 10^{43} erg s^{-1}. The distance between the tick marks is 5 arcsec.

All uncertainties for the density measurements so far were calculated assuming only Poissonian noise with a sample variance $\sigma_N = \sqrt{N}$, where N is the number of galaxies. Cosmic variance (CV) due to galaxy clustering can exceed sample variance and is dependent on the survey geometry. Although our survey volume is quite large and the CV might be not significant, we also provide the density measurements with uncertainties arising from CV.

We use the CV Calculator (Trenti & Stiavelli 2008) to estimate the CV for our survey volume. Given our survey configuration and a sample completeness of 95%, assuming a halo filling factor of 1, we obtain a relative error due to CV of 25.7% for our survey geometry. The fractional error due to Poissonian shot noise is 7.4%. Adding these errors in quadrature, the resulting relative error is approximately 26.7%. Taking this error into consideration, the average surface density over the whole field is $(7.4 \pm 1.9) \times 10^{-2}$ arcmin^{-2} Δz^{-1}.

4.2. Comparison with Previous Wide-field LAE Surveys

We compare our LAE number densities with those of other surveys at similar redshifts (Palunas et al. 2004; Prescott et al. 2008; Nilsson et al. 2009; Guaita et al. 2010; Mawatari et al. 2012). Since each survey employs different selection criteria in EW and NB magnitude (Lyα luminosity), as well as probes different redshift depths due to different filter widths, we need to correct the reported LAE surface density values in the literature. We scale the LAE surface densities assuming Lyα luminosity functions $\phi(L)$ at $z = 2$–3 and an exponential EW distribution (e^{-w/w_0}) with a scale length of w_0. We calculate the following correction factors for each survey:

$$C_L = \frac{\int_{L_0}^{\infty} \phi(L')dL'}{\int_{L_i}^{\infty} \phi(L')dL'}, \quad (4)$$

$$C_{\rm EW} = \frac{\int_{{\rm EW}_0}^{\infty} \exp(-w'/w_0)dw'}{\int_{{\rm EW}_i}^{\infty} \exp(-w'/w_0)dw'}, \quad (5)$$

$$C_{\Delta z} = \Delta z_0/\Delta z_i, \quad (6)$$

where C_L, $C_{\rm EW}$, and $C_{\Delta z}$ are the correction factors for Lyα luminosity, EW, and redshift depth, respectively; L_i, EW$_i$, and Δz_i are the luminosity limits, EW cuts, and redshift depths for different surveys, respectively; and L_0, EW$_0$, and Δz_0 are the values used in our survey. We adopt the results from Gronwall et al. (2007) for the Schechter function, assuming no redshift evolution: $L^* = 10^{42.66}$ erg s^{-1}, $\Phi^* = 1.28 \times 10^{-3}$ Mpc^{-3},

Table 2
Properties of Lyα Blobs

Object	R.A. (J2000)	Decl. (J2000)	L(Lyα) (10^{43} erg s^{-1})	Size (arcsec^2)	Recovery Fraction
Boötes-LAB1	14 30 59.0	+35 33 24	2.70 ± 0.10	43 ± 4.8	···
Boötes-LAB2	14 30 57.8	+35 34 31	1.61 ± 0.08	29 ± 6.9	···
Boötes-LAB5	14 32 17.7	+35 47 53	1.360 ± 0.098	15.5 ± 1.7	97.5%
Boötes-LAB6	14 30 50.2	+35 41 03	0.931 ± 0.129	16.1 ± 2.3	96.2%
Boötes-LAB7	14 30 13.0	+35 37 45	1.261 ± 0.094	15.6 ± 1.6	93.9%

Note. We adopt a naming convention such that the four Lyα blobs in the original wide and shallow survey (Yang et al. 2009) are Boötes-LAB1 to Boötes-LAB4 and that the three new Lyα blobs found in this study are Boötes-LAB5 to Boötes-LAB7. Note that Boötes-LAB3 and Boötes-LAB4 are not included in the table because they were not covered by this new survey. Blobs are listed in the order of recovery fraction.

(This table is available in machine-readable form.)

and $\alpha = -1.36$, and $w_0 = 74$ Å. We summarize the results from the previous LAE surveys, the adopted correction factors, and the LAE surface densities corrected to our survey properties in Table 3.

In Figure 7, we show the surface density values from other surveys, with redshifts close to $z = 2.3$, and compare their measurements with our peak and average surface densities. Our average surface densities agree with those of Nilsson et al. (2009), Mawatari et al. (2012), and Guaita et al. (2010). The LAE density of our overdense region with a radius of 10 Mpc is in agreement with average density values from the two surveys that targeted known dense regions, Palunas et al. (2004) and Prescott et al. (2008), who targeted the J2143–4423 protocluster at $z = 2.38$ and the LABd05 protocluster (Dey et al. 2005), respectively.

Given that the LF and EW distribution might evolve between $z = 2$ and 3 (Ciardullo et al. 2012), we also test how the correction factors C_L, $C_{\rm EW}$, and $C_{\Delta z}$ might be affected by the redshift evolution of the luminosity function. We repeat the previous comparison using the luminosity function of Guaita et al. (2010) for $z = 2$ with $L^* = 10^{42.33}$ erg s^{-1}, $\Phi^* = 0.64 \times 10^{-3}$ Mpc^{-3}, and $\alpha = -1.65$. The resulting surface density values differ by ∼30% on average and by at most 70% from the values in Table 3 (Figure 7). Note that we do not show the values for the shallowest Palunas et al. (2004) survey because its sources populate only the bright end of the luminosity function, which introduces large errors when extrapolated to the faint end.

4.3. Measurement of Surface and Volume Overdensity

To gauge the significance of the discovered overdense structure, and to compare its properties with the cosmological simulations and other known protoclusters, we estimate the surface and volume *over*density in this section.

The surface density contrast $\delta_\Sigma = (\Sigma_{\rm overdense} - \bar{\Sigma})/\bar{\Sigma}$ is 2.7 inside a 8.1 Mpc (5′) radius around the position of peak density. This value increases to $\delta_\Sigma = (\Sigma_{\rm overdense} - \Sigma_{\rm field})/\Sigma_{\rm field} = 4.1$ if we compare our overdense region to the *field* density ($\Sigma_{\rm field}$). Throughout the paper and to be consistent with the definition of density contrast used in the literature, we use the average density of the whole survey (i.e., $\bar{\Sigma}$) when calculating overdensities. Calculating contrast densities instead of using the average field (i.e., $\Sigma_{\rm field}$) value would increase the peak overdensity, while the standard definition yields a more conservative result.

Assuming that the overdense region is a sphere with a radius of 10 Mpc, we can estimate the volume density contrast as follows. We find 35 LAEs inside a projected area with a 10 Mpc radius centered on R.A. = $14^{\rm h}30^{\rm m}31\overset{\rm s}{.}3$, decl. = +35° 25′01, while only ∼9 LAEs are expected given the average volume density over the survey. Thus, we estimate that ≈26 more LAEs are located within the assumed spherical overdensity having a volume of $\approx 4.18 \times 10^3$ Mpc^3. Our survey contains 183 objects in a volume of 3.0×10^5 Mpc^3. The volume density contrast $\delta = (\rho_{\rm overdense} - \bar{\rho})/\bar{\rho}$ is then ∼ 10.4, where $\rho_{\rm overdense}$ is the density inside the spherical region, and $\bar{\rho}$ is the average density over the whole survey.

Several other surveys also find LAE overdensities at $z \simeq 2 - 4$. At $z = 2.16$, a protocluster with an overdensity of $\delta_\Sigma \sim 3$ is associated with the PKS 1138–262 radio galaxy and its extended Lyα halo (Kurk et al. 2000; Venemans et al. 2007). Targeting a known cluster, J2143–4423, at $z = 2.38$, Palunas et al. (2004) found an LAE overdensity of $\delta_\Sigma \simeq 2$. A similar surface overdensity of $\delta_\Sigma \sim 2$ was seen by Prescott et al. (2008) around a known LAB at $z = 2.7$. An overdensity was found by Saito et al. (2015) around the radio galaxy TN J1338-1942 at redshift 3.1, with $\delta_\Sigma = 2.8 \pm 0.5$. At $z = 3.78$, two or three overdensities with similar δ_Σ values were found by Lee et al. (2014) and Dey et al. (2016), with $\delta_\Sigma = 2.5$–2.8. The largest overdensity by far lies in the SSA22 field (Steidel et al. 2000), with a surface density contrast $\delta_\Sigma = 5 \pm 2$ (Steidel et al. 2000; Matsuda et al. 2004, 2005; Yamada et al. 2012). More recently, Cai et al. (2017b) discovered a massive overdensity at $z = 2.3$, having a spectroscopically confirmed volume density contrast of $\delta \sim 10$, associated with an extremely large and luminous Lyα nebula (Cai et al. 2017a). All these surveys probe redshift slices of $\Delta z \sim 0.03 - 0.16$, similar to our own $\Delta z = 0.037$ redshift depth. Although it is difficult to directly compare these overdensity contrasts with our own values because of different kernels and field sizes, as well as different Δz's, the δ_Σ and δ of our overdensity are roughly comparable to these protocluster candidates.

4.4. Will Boötes J1430+3522 Evolve into a Cluster Today?

Using Lyα emitters as a density tracer, we discover an overdense region with a projected surface density of $\delta_\Sigma = 2.7 \pm 1.1$ and a radius of ∼10 Mpc. To address whether this structure could collapse into a virialized galaxy cluster by $z = 0$, i.e., whether it is in fact a "protocluster," we compare our observations with the analysis of structure

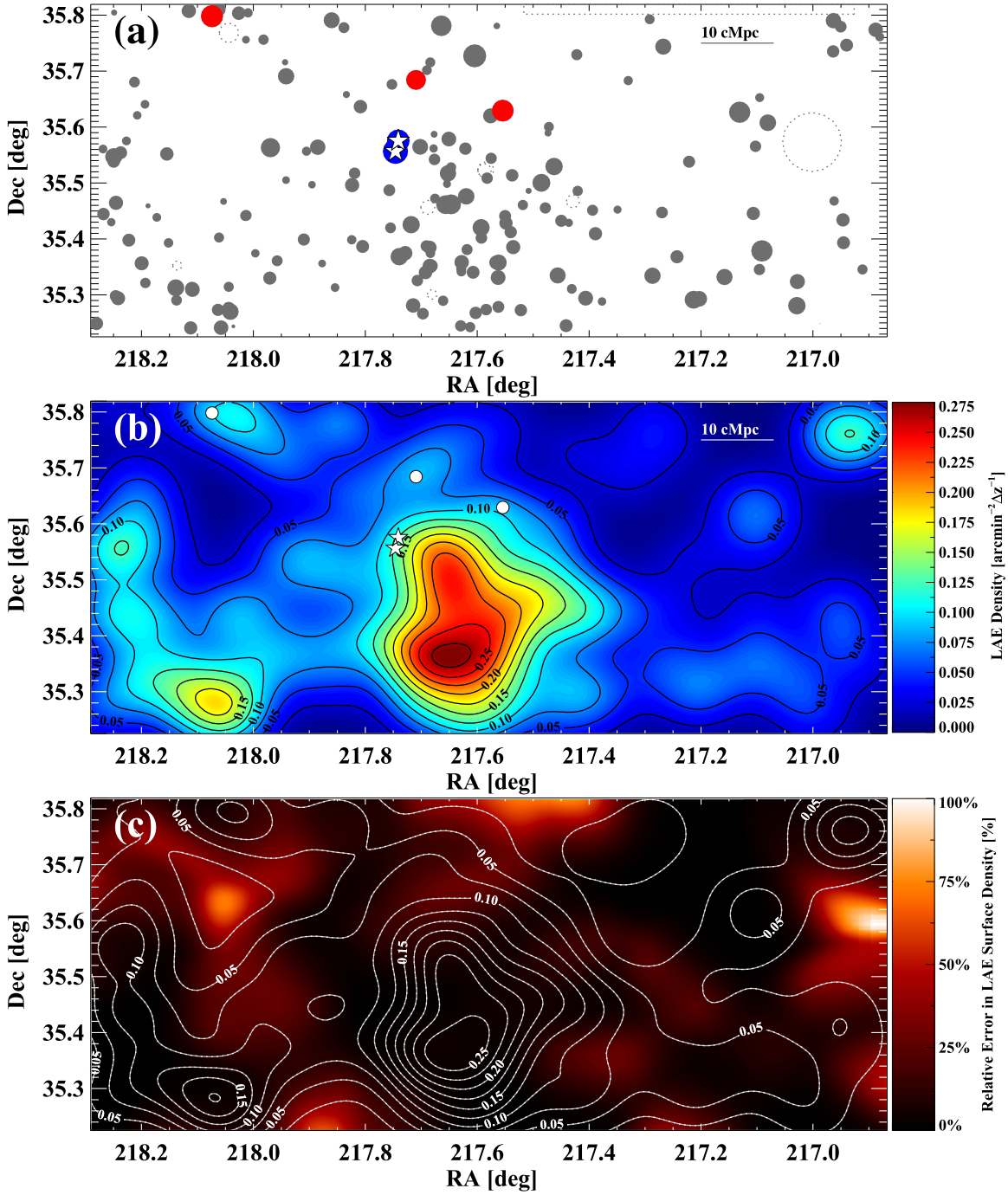

Figure 5. (a) Spatial distribution of 183 Lyα emitters and blobs. The filled gray and red circles represent Lyα emitters and new Lyα blob candidates, respectively. The star symbols are the two previously known Lyα blobs (Yang et al. 2009). The radii of the circles are proportional to the logarithm of the Lyα emitters' luminosities, in the range of $10^{4}1.4$–43.4 erg s^{-1}. The field of view is $69\farcm3 \times 35\farcm5$ (138.5 Mpc $\times$ 57.5 Mpc). The dotted lines enclose areas that have been excluded from our analysis because of contamination from bright stars or galaxies. (b) Lyα emitter surface density distribution obtained from the KDE method explained in the Appendix. The contour labels show the surface density of Lyα emitters in arcmin^{-2} per$\Delta z = 0.037$—the value given by the narrowband filter width. The two known Lyα blobs are marked with stars. The overdense region is clearly visible toward the center of the image. (c) Average and scatter of the Lyα-emitter surface density of the 81 surface density maps corresponding to different selection methods. The contour labels represent the average surface density, while the background image represents the scatter around this average map, in percentages. The scatter is largest away from the overdense region, increasing the confidence that the shape and size are not significantly affected by varying the selection criteria.

formation from cosmological simulations by Chiang et al. (2013).

Using the Millennium Run (MR; Springel et al. 2005) cosmological simulation, Chiang et al. (2013) identified the mass, extent, and density contrast that galaxy cluster progenitors must have in order to evolve into galaxy clusters at $z = 0$. In their study, a cluster is defined as a virialized dark matter halo with a total mass greater than $10^{14}\,M_{\odot}$ at redshift $z = 0$. Based on this definition they tracked the evolution of DM halos and galaxies in ~3000 clusters from early epochs ($z = 7$) to the present day. For this sample, they calculated the correlation between galaxy density contrast of protoclusters at

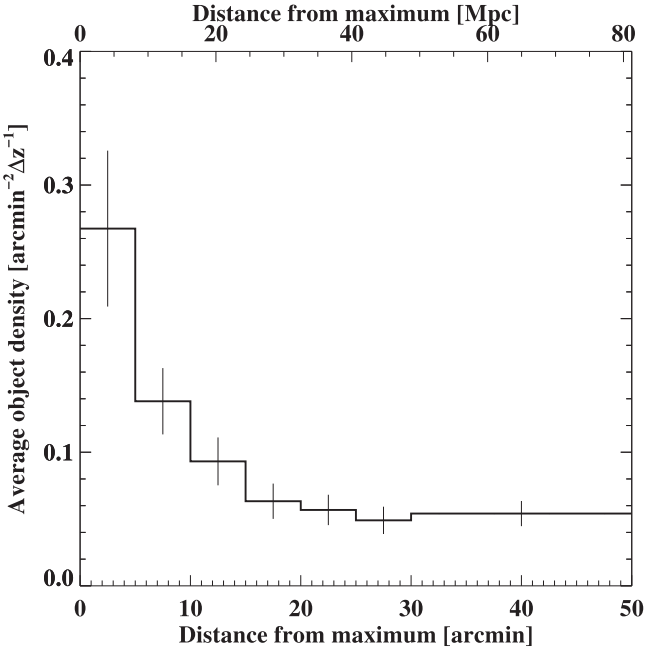

Figure 6. Radial profile of the surface density peak, as a function of distance from the center of the overdense region, using 5′ bins for the denser regions, and one 20′ bin at the edge of the field. The peak surface density is 0.27 arcmin^{-2} Δz^{-1}, decreasing to the field value of $(5.4 \pm 0.9) \times 10^{-2}$ arcmin^{-2} Δz^{-1} at $r > 30$ Mpc (20′) from the peak. The average surface density over our entire survey is $(7.4 \pm 0.54) \times 10^{-2}$ arcmin^{-2} Δz^{-1}. The overdense region has a radius of 10 Mpc, a surface density contrast of $\delta_\Sigma = 2.7$, and a volume density contrast value of $\delta = 10.4$.

different redshifts and the mass of its present-day cluster offspring. They also showed how the projected density contrast is affected by the redshift uncertainty Δz of a survey, demonstrating that potential protocluster overdensities become observationally indistinguishable from the field, for all except the most massive structures, if the overdensities are measured with $\Delta z > 0.1$. Thus, wide-field narrowband imaging surveys are the key to identifying early stages of cluster formation.

In their analysis, Chiang et al. (2013) measure the density contrast of the structures in the MR data after smoothing it with $(15\ \mathrm{Mpc})^3$ and $(25\ \mathrm{Mpc})^3$ tophat cubic kernels. To match these kernel sizes, we smooth our survey map with $(15 \times 15 \times \Delta z)$ Mpc^3 and $(25 \times 25 \times \Delta z)$ Mpc^3 rectangular windows, with a redshift uncertainty of $\Delta z = 0.037$ (46.6 Mpc). In this configuration, we find $\delta_{\Sigma,15} = 3.4$ and $\delta_{\Sigma,25} = 2.0$ for Boötes J1430+3522.

According to Chiang et al. (2013), an uncertainty of $\Delta z \approx 0.037$ (46.6 Mpc) in the redshift of the Lyα emitters used to trace an overdensity at redshift $z = 2$–3 reduces the apparent surface density contrast by ∼50% compared to its original value calculated using $(15\ \mathrm{Mpc})^3$ cubic windows. This is because with increasing redshift uncertainties, more galaxies in the background and the foreground of the overdense regions are included in the analysis and smooth out irregularities in surface density. Correcting for this effect, we obtain a $\delta_{15,\mathrm{corrected}} \approx 6.8$. Note that if we assume that the overdensity is confined only within the $(15\ \mathrm{Mpc})^3$ cube, $\delta_{15,\mathrm{corrected}} = 10.6$ would be required to yield the observed $\delta_{\Sigma,15} = 3.4$. Therefore, $\delta_{15,\mathrm{corrected}} \approx 6.8$ should be a reasonable value for the density contrast over the $(15\ \mathrm{Mpc})^3$ cubic window.

This density contrast is much higher than $\delta_{15} = 2.88$, the value needed for a $z \sim 2$ structure to evolve into a cluster at $z = 0$ with >80% probability (Chiang et al. 2013). Here, we have adopted δ_{15} using galaxies with SFR $> 1\ M_\odot\ \mathrm{yr}^{-1}$, which are analogs to Lyα-emitter populations. This $\delta_{15,\mathrm{corrected}}$ is high enough for it to evolve into a present-day cluster with near 100% certainty, even if a wide range of other tracer populations are assumed (see Figure 8 of Chiang et al. 2013). Therefore, we conclude that Boötes J1430+3522 is indeed a "protocluster."

Finally, using the correlation found by Chiang et al. (2013) between galaxy contrast at a given epoch and present-day cluster mass, we estimate the future mass protocluster to be $\log(M/M_\odot) \sim 15.1 \pm 0.2$ similar to that of Coma cluster.

4.5. Size and Amplitude of Protoclusters

We have discovered a new protocluster traced by LAEs and Lyα blobs. To compare it to other known protoclusters, we compile previous narrowband imaging surveys at $z = 2$–3 that have discovered both Lyα blobs and protoclusters in the same field. These three protoclusters are located in the E-CDFS (Yang et al. 2010), the 53W002 (Mawatari et al. 2012), and SSA22 fields (Matsuda et al. 2011; Yamada et al. 2012) at $z = 2.3$, 2.4, and 3.1, respectively.[4]

We reproduce the surface density maps of Lyα emitters and blobs for these three fields and Boötes J1430+3522 field in Figure 8. To make these maps, we use the KDE and cross-validation method presented in this paper with Gaussian kernel widths of $\sigma = 1\farcm43$, $1\farcm55$, $1\farcm87$, and $2\farcm64$ for the 53W002, E-CDFS, SSA22, and Boötes J1430+3522 fields, respectively. These kernel sizes are within 25% of the values originally adopted by each survey: $\sigma = 1\farcm5$ for 53W002 (Mawatari et al. 2012), $1\farcm2$–$2\farcm2$ for E-CDFS (Yang et al. 2010), and $1\farcm5$ for SSA22 (Yamada et al. 2012). To test the effect of kernel sizes on our results below, we also produce maps with (1) the values adopted in each reference and (2) a same width ($1\farcm5$) for all four fields. Our results here do not change with the choice of the kernel size.

Figure 8 shows the contours of surface overdensity $\delta_\Sigma = (\Sigma - \bar{\Sigma})/\bar{\Sigma}$ for each survey. When calculating δ_Σ, we estimate $\bar{\Sigma}$ over each survey. For the E-CDFS protocluster (Balestra et al. 2010; Yang et al. 2010,) which almost fills the $30' \times 30'$ field, we use the $\bar{\Sigma}$ from our Boötes survey because both surveys used the same narrowband filter and sample-selection methods.

Figure 8 shows that both the peak amplitudes and the sizes of the protoclusters are consistent with each other, despite the wide ranges of survey areas probed in each survey. In particular, three protoclusters in the E-CDFS, Boötes J1430+3522, and SSA22 fields have almost identical peak surface density contrasts of $\delta_\Sigma = 2.8$–3.0. In contrast, the 53W002 protocluster has a smaller size and lower peak amplitude than the others, suggesting it is only moderately rich. The three protoclusters (E-CDFS, Boötes J1430+3522 and SSA22) have 8.5–10 physical Mpc diameters (28–39 comoving Mpc; 17′–21′) if we measure the largest dimension of the $\delta_\Sigma = 1$ contour (dashed). The linear size of the protocluster does not grow bigger than this typical size, even though the survey area increases from E-CDFS (35′), Boötes J1430+3522 (70′) to the

[4] Prescott et al. (2008) and Erb et al. (2011) also found Lyα blobs associated with overdensities traced by LAEs. However, the coordinates of the LAEs in their fields are not available, and it is unknown if the small survey area (220 arcmin^2) of Erb et al. (2011) includes the whole overdensity.

Table 3
Comparison with Other LAE Surveys

Survey (1)	z (2)	Δz (3)	EW Cut (4)	L(Lyα) (5)	$C_{\Delta z}$ (6)	$C_{\rm EW}$ (7)	C_L (8)	$\bar{\Sigma}$ (9)
Nilsson et al. (2009)	2.2	0.1061	20	42.36	0.364	1.000	1.565	0.107
Guaita et al. (2010)	2.1	0.0411	20	41.80	0.940	1.000	0.415	0.075
Mawatari et al. (2012)	2.4	0.0683	25	41.99	0.566	1.121	0.611	0.107
Prescott et al. (2008)	2.7	0.1653	40	42.18	0.234	1.580	0.955	0.350
Palunas et al. (2004)	2.3	0.0444	36	42.78	0.870	1.475	8.958	0.201
This Work	2.3	0.0370	20	42.19	...	...	...	0.074

Note. (1) reference for the survey, (2) survey redshift, (3) redshift depths from filter widths, (4)–(5) selection criteria for EWs (Å) and Lyα luminosity ($\log[L/\mathrm{erg\ s^{-1}}]$), (6)–(8) correction factors for the redshift depth, EW, and Lyα luminosity, introduced in Section 4.2, (9) average surface density ($\mathrm{arcmin^{-2}}\ \Delta z^{-1}$) over the entire field corrected for our sample-selection criteria.

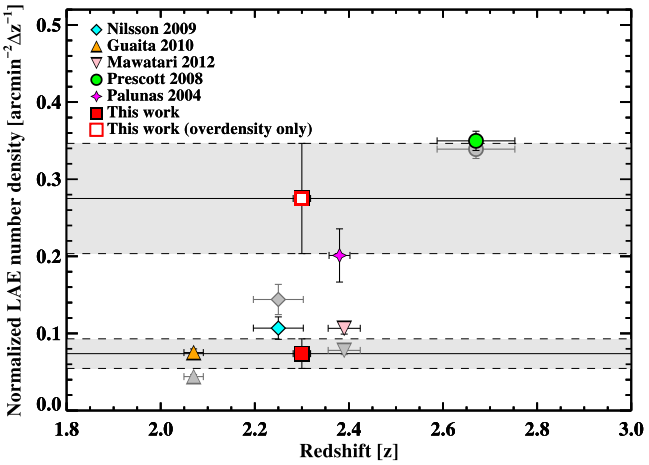

Figure 7. Surface densities of LAEs, after correcting for the different selection criteria of each survey, using the $z = 3.1$ luminosity function from Gronwall et al. (2007). The gray symbols represent the same surface densities corrected instead using the $z = 2.1$ luminosity function of Guaita et al. (2010). Since our survey extends well beyond the overdense region, we consider the average surface density over the whole field (filled square) and for the overdensity (open square) separately. The gray bands show the 1σ range about each value. Note that our overdensity is consistent with that of known dense regions targeted by Palunas et al. (2004) and Prescott et al. (2008).

SSA22 field (110′). For $\delta_\Sigma = 2$ (dotted–dashed) contour, the protoclusters also have similar sizes of 4.6–7.2 physical Mpc (16–24 comoving Mpc) with wider ranges.

Protocluster overdensity profiles from simulations (Chiang et al. 2013) show that even for the most massive protoclusters at redshift $z = 2$–3 (i.e., progenitors of galaxy clusters with a present-day mass greater than $10^{15}\,M_\odot$), the average diameters of areas with a volume density contrast above $\delta = 1$ and 2 are ≈32 and ≈24 Mpc, respectively. Although it is not straightforward to relate the size measured for a fixed surface density contrast (δ_Σ) to that measured for a volume density contrast (δ), these sizes are in good agreement with the observations discussed above.

The comparable extents of protoclusters at $z = 2$–3, and the fact that their observed sizes do not grow with the extent of the surveyed field, suggest that they are the largest bound structures at that epoch. It is clear from our results that a very wide-field survey over ∼1 degree is required to reliably confirm massive protoclusters at this epoch and to determine their full physical sizes.

4.6. Lyα Blobs in Protocluster Outskirts

Visually, all the maps in Figure 8 are striking; the Lyα blobs often lie outside the densest concentration of LAEs. Mawatari et al. (2012) also note that all four of their LABs are located on the edges of high-density regions. To quantify relative, local environments of Lyα emitters and blobs, we measure their local overdensities from the smoothed surface density maps (Figure 9). The distribution of LAEs' local overdensities is similar to the lognormal distribution that is known to approximate the dark matter distribution (e.g., Coles & Jones 1991; Orsi et al. 2008). The two-sample Kolmogorov–Smirnov test shows that the distributions of the LAE and LAB populations are different at the 3.8σ significance level. The distributions differ most at moderate overdensities, $\delta_\Sigma = 1$–2, where there is a clear excess of Lyα blobs. While it is not reanalyzed here, the LABd05 blob is also located near the region of $\delta_\Sigma \sim 1.3$ (Prescott et al. 2008; see their Figure 3). Likewise, the six Lyα blobs in Erb et al. (2011) appear to lie at the edges of the HS 1700+643 protocluster field. We conclude that Lyα blobs prefer moderately overdense regions of LAEs that are twice or three times denser than the average density of the survey ($\delta_\Sigma \approx 0$), perhaps avoiding the densest regions within a protocluster.

Why do Lyα blobs occupy the moderate overdense region or outskirts of protoclusters? One possibility is that Lyα blobs represent protogroups that are accreting into a more massive protocluster from the cluster outskirts. Prescott et al. (2012) found that the LABd05 Lyα blob (Dey et al. 2005) contains numerous compact, small, low-luminosity ($<0.1L_*$) galaxies. Similarly, Yang et al. (2011, 2014b) identified several Hα or [O III] emitting sources within Lyα blobs with relative line-of-sight velocity differences of ∼200–400 km s^{-1}, which are consistent with the velocity dispersions of $\sim 10^{13}\,M_\odot$ galaxy groups. Furthermore, the number and variance of Lyα blobs is consistent with them occupying $\sim 10^{13}\,M_\odot$ halos. We speculate that the extended Lyα-emitting gas may be the proto-intragroup medium and/or stripped gas originating from galaxy–galaxy interactions within these protogroups.

We test the plausibility of this scenario by checking if the expected number of protogroups in the massive protocluster environment is roughly consistent with that of the Lyα blobs around Boötes J1430+3522. We estimate that our LAE overdensity will evolve into a $\sim 10^{15}\,M_\odot$ rich cluster today (Section 4.4). In this case, simulations predict that the current protocluster mass is $\sim 10^{14}\,M_\odot$ and that it accretes $\sim 15\,10^{13}\,M_\odot$

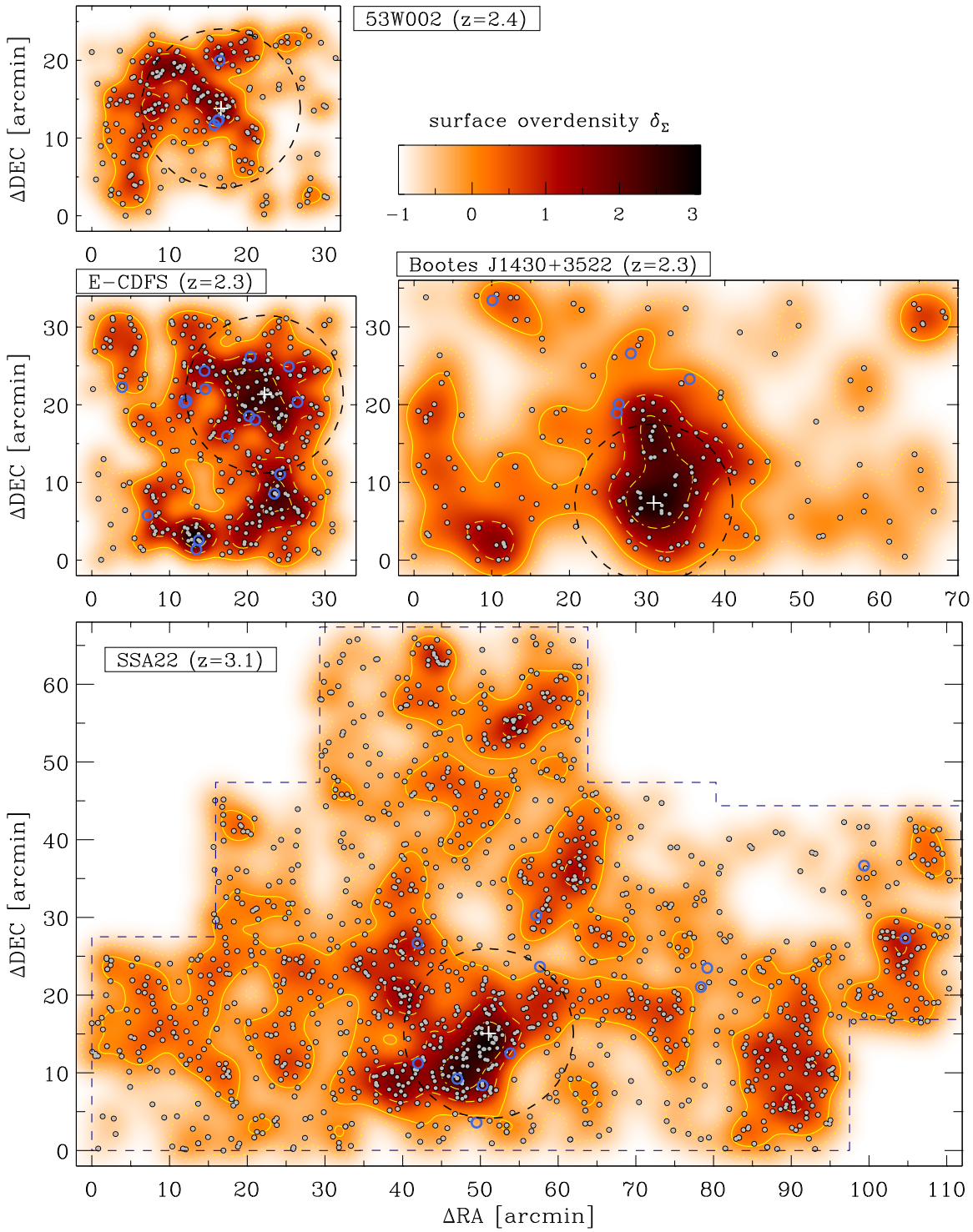

Figure 8. Surface overdensity maps for four survey fields: 53W002 (Mawatari et al. 2012), E-CDFS (Yang et al. 2010), Boötes J1430+3522 (this work), and SSA22 (Matsuda et al. 2011; Yamada et al. 2012). Lyα emitters and blobs are marked with gray dots and blue open circles, respectively. Four contours (dot, solid, dashed, dotted–dashed) represent $\delta_\Sigma = (\Sigma - \bar{\Sigma})/\bar{\Sigma} = -0.5$, 0, 1, and 2, respectively. The dashed black circles are centered on the highest peaks of each region with a radius of 5 physical Mpc. The Lyα blobs often live on the outskirts of the highest peaks. The sizes and the peak amplitudes of the overdensities are consistent from field to field; three overdensities in the E-CDFS, Boötes J1430+3522, and SSA22 fields have 8.5–10 physical Mpc diameters for the $\delta_\Sigma = 1$ contour (dashed) and the peak $\delta_\Sigma = 2.8$–3.0. Note that the sizes of the overdensities do not increase with survey size, which is consistent with them being the largest overdensities at this epoch and evolving into the richest clusters today.

halos from $z \sim 2.3$ to 0 (Gao et al. 2004; Giocoli et al. 2008; Jiang & van den Bosch 2016). Thus, the five Lyα blobs that we detect within ~10 Mpc (~5 virial radii) could plausibly trace some of the group-like halos that build the cluster.

5. Conclusions

We carry out a deep narrowband imaging survey of a $\sim 1^\circ \times 0.^\circ 5$ region at $z = 2.3$ around a known bright Lyα blob pair discovered by a blind narrowband survey (Yang et al.

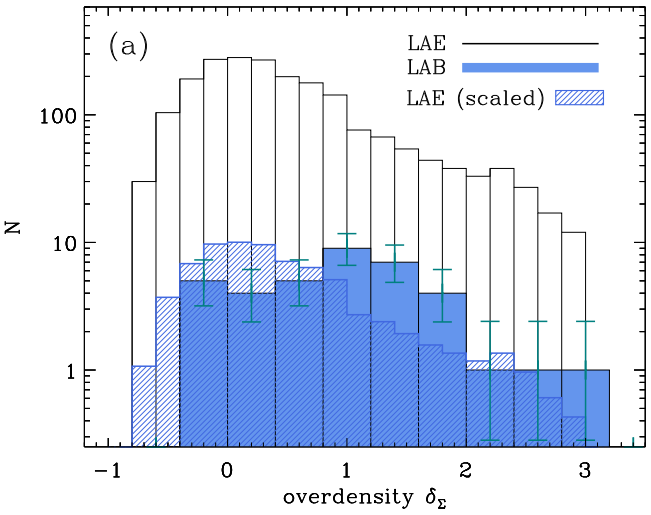

Figure 9. Distribution of surface overdensity δ_Σ for Lyα emitters (open histogram) and Lyα blobs (blue filled histogram). The shaded histogram is the open histogram scaled down for easier comparison with the Lyα blob distribution. The Lyα blob distribution shows a relative excess at $\delta_\Sigma = 1$–2, suggesting that they favor moderately overdense regions of LAEs.

2009). We test whether bright Lyα blobs are indeed a tracer of overdense regions at high redshift.

We find a total of 183 Lyα emitters, including three new intermediate Lyα blobs in our $69\farcm3 \times 35\farcm4$ field. The average Lyα-emitter surface density in our field is $\bar{\Sigma} = (7.4 \pm 1.9) \times 10^{-2}$ arcmin^{-2} Δz^{-1}, corresponding to a volume density $n = (6 \pm 1.5) \times 10^{-4}$ Mpc^{-3} over the survey volume of 3.03×10^5 Mpc^3. The surface density varies from 5.4×10^{-2} arcmin^{-2} Δz^{-1} in the field region to 0.27 arcmin^{-2} Δz^{-1} at the densest part, in good agreement with results from previous surveys that targeted either field regions or protoclusters at similar redshifts.

We discover a massive overdensity (Boötes J1430+3522) of Lyα emitters with a surface density contrast of $\delta_\Sigma = 2.7 \pm 1.1$, a volume density contrast of $\delta \sim 10.4$, and a projected diameter of $\approx$20 comoving Mpc. By comparing our measurements with an analysis of the MR cosmological simulation (Chiang et al. 2013), we conclude that this large-scale structure is indeed a protocluster and is likely to evolve into a present-day Coma-like galaxy cluster with $\log(M/M_\odot) \sim 15.1 \pm 0.2$.

In our survey and three others we re-analyze here, the physical extent and peak amplitude of the LAE overdensities are consistent across the surveys. Because these properties do not increase with survey size, it is likely these overdensities are the largest structures at this epoch and will indeed evolve into rich clusters today.

The discovery of a protocluster in the vicinity of the two Lyα blobs, along with the discovery of three new nearby LABs, confirms that bright Lyα blobs are associated with overdense regions of LAEs. Yet, among the four surveys we analyze, LABs tend to avoid the innermost, densest regions of LAEs and are preferentially located in the outskirts at density contrasts of $\delta_\Sigma = 1$–2. This result, and the likelihood that blobs themselves occupy $\sim 10^{13}\,M_\odot$ individual halos (Yang et al. 2010), suggest, that Lyα blobs represent protogroups that will be accreted by the protocluster traced by LAEs. In that case, the extended Lyα-emitting blob gas may be a precursor of the intragroup medium, and ultimately a contributor to the intracluster medium.

We thank the anonymous referee for her or his thorough reading of the manuscript and helpful comments. We thank Lucia Guaita for providing the Lyα-emitter catalogs, and Ashoordin Ashoormaran for his insights on the sub-halo mass function. T.B. and Y.Y. acknowledge support from the BMBF/DLR grant No. 50 OR 1306. Y.Y.'s research was supported by Basic Science Research Program through the National Research Foundation of Korea (NRF) funded by the Ministry of Science, ICT & Future Planning (NRF-2016R1C1B2007782). Support for B.M. was provided by the DFG priority program 1573 "The physics of the interstellar medium." T.B., A.K., and F.B. acknowledge support by the Collaborative Research Council 956, sub-project A1, funded by the Deutsche Forschungsgemeinschaft (DFG). A.I.Z. acknowledges support from NSF grant AST-0908280 and NASA grant NNX10AD47G.

Appendix
Estimating LAE Surface Density Using KDE and Cross-validation

To build a continuous Lyα-emitter density map (Figure 5(b)) from the spatial distribution of Lyα emitters (Figure 5(a)), we use the KDE method (Rosenblatt 1956; Parzen 1962) with a cross-validation technique. Assuming that the sky positions of our Lyα-emitter sample $\{\boldsymbol{x}_1, \boldsymbol{x}_2, \ldots, \boldsymbol{x}_N\}$ are randomly drawn from an underlying unknown surface density distribution $f(\boldsymbol{x})$, our goal is to find an estimator $\hat{f}(\boldsymbol{x})$ for the true distribution. Using KDE

$$\hat{f}(\boldsymbol{x}) = \sum_{j=1}^{N} K(\boldsymbol{x} - \boldsymbol{x}_j; \boldsymbol{\sigma}_j), \tag{7}$$

where $K(\boldsymbol{x}; \boldsymbol{\sigma})$ is a normalized kernel, e.g., in a functional form of uniform, triangular, or Gaussian. The σ is a bandwidth, a free-smoothing parameter that strongly influences the estimate obtained from KDE. Note that σ can be 1D or 2D, as well as different for each datum. In our application, we consider 1D and 2D Gaussian kernels:

$$K(\boldsymbol{x}; \boldsymbol{\sigma}) = \frac{1}{\sqrt{2\pi}\,\sigma} \exp\left[-\frac{x^2}{2\sigma^2}\right], \tag{8}$$

$$K(\boldsymbol{x}; \boldsymbol{\sigma}) = \frac{1}{2\pi\sigma_x\sigma_y} \exp\left[-\frac{x^2}{2\sigma_x^2} + \frac{y^2}{2\sigma_y^2}\right]. \tag{9}$$

Our goal is to determine the σ that best describes the data itself. KDE is mathematically identical to smoothing a map image with a Gaussian kernel, the approach most often taken in the literature, although the smoothing widths are often chosen rather arbitrarily. We show below that an optimal σ can be determined from the data themselves. For that purpose, we use a leave-one-out cross-validation scheme (e.g., Hogg 2008): let $\hat{f}_{-i}(\boldsymbol{x})$ be the KDE of f that is obtained from our sample, excluding the ith element. The probability of finding that ith element at the observed position $\boldsymbol{x}_i$ is proportional to $\hat{f}_{-i}(\boldsymbol{x}_i)$:

$$\hat{f}_{-i}(\boldsymbol{x}_i) = \sum_{j=1;j\neq i}^{N} \frac{1}{\sqrt{2\pi}\,\sigma} \exp\left[-\frac{||\boldsymbol{x}_i - \boldsymbol{x}_j||^2}{2\sigma^2}\right]. \tag{10}$$

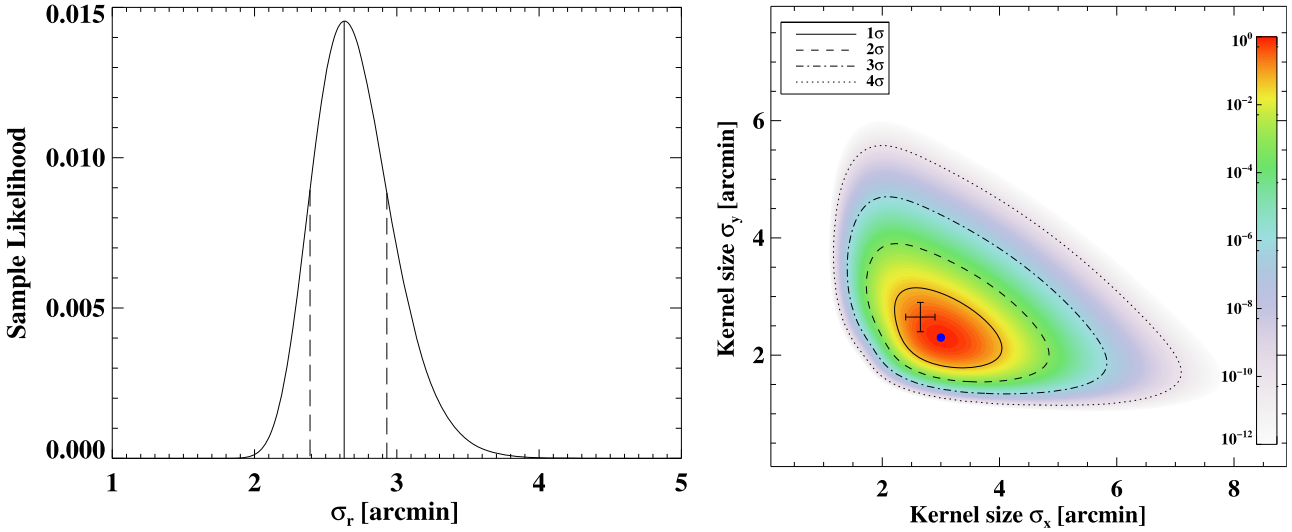

Figure 10. (Left) Sample likelihood function against the width of the circular Gaussian smoothing kernel σ. The vertical line marks the position of the maximum likelihood at $\sigma = 2\farcm63$, while the dashed lines indicate the 1-σ uncertainties in kernel size. (Right) Values of the sample likelihood as a function of 2D smoothing kernel sizes. The axes show the values of the 2D Gaussian kernel widths, σ_x and σ_y, used for kernel density estimation. The color levels indicate the values of the likelihood, where the dot represents its maximum value, while the data point with error bars indicates the size of a circular Gaussian kernel with $\sigma = 2\farcm63$.

We then find the parameters that best *predict* the observed data by maximizing the likelihood of finding all $\{\boldsymbol{x}_i\}$ for a given σ:

$$L(\{\boldsymbol{x}_i\}_{i=1}^{N}|\sigma) = \prod_{i=1}^{N} \hat{f}_{-i}(\boldsymbol{x}_i). \quad (11)$$

We use a simple grid search to determine the kernel width σ. Figure 10 shows the likelihood L as a function of σ for an 1′–5′ range. The maximum likelihood is obtained for $\sigma = 2.63^{+0.30}_{-0.24}$′. If we adopt a 2D Gaussian kernel with two smoothing parameters (σ_x, σ_y) as in Equation (9), $\sigma_x = 3.00^{+1.03}_{-0.78}$′ and $\sigma_y = 2.31^{+0.83}_{-0.52}$′. The 1D kernel width is within the 68.3% confidence interval of 2D kernel width. We use $\sigma = 2\farcm63$ throughout the paper to estimate the underlying density distribution.

ORCID iDs

Toma Bădescu https://orcid.org/0000-0001-7332-0505
Yujin Yang https://orcid.org/0000-0003-3078-2763
Frank Bertoldi https://orcid.org/0000-0002-1707-1775
Ann Zabludoff https://orcid.org/0000-0001-6047-8469
Alexander Karim https://orcid.org/0000-0002-8414-9579
Benjamin Magnelli https://orcid.org/0000-0002-6777-6490

References

Balestra, I., Mainieri, V., Popesso, P., et al. 2010, A&A, 512, A12
Bertin, E., & Arnouts, S. 1996, A&AS, 117, 393
Bleem, L. E., Stalder, B., de Haan, T., et al. 2015, ApJS, 216, 27
Boylan-Kolchin, M., Springel, V., White, S. D. M., Jenkins, A., & Lemson, G. 2009, MNRAS, 398, 1150
Cai, Z., Fan, X., Bian, F., et al. 2017a, ApJ, 839, 131
Cai, Z., Fan, X., Yang, Y., et al. 2017b, ApJ, 837, 71
Cantalupo, S., Porciani, C., Lilly, S. J., & Miniati, F. 2005, ApJ, 628, 61
Capak, P. L., Riechers, D., Scoville, N. Z., et al. 2011, Natur, 470, 233
Cen, R., & Zheng, Z. 2013, ApJ, 775, 112
Chiang, Y.-K., Overzier, R., & Gebhardt, K. 2013, ApJ, 779, 127
Ciardullo, R., Gronwall, C., Adams, J. J., et al. 2013, ApJ, 769, 83
Ciardullo, R., Gronwall, C., Wolf, C., et al. 2012, ApJ, 744, 110
Coles, P., & Jones, B. 1991, MNRAS, 248, 1
Cooke, E. A., Hatch, N. A., Muldrew, S. I., Rigby, E. E., & Kurk, J. D. 2014, MNRAS, 440, 3262
Daddi, E., Dannerbauer, H., Stern, D., et al. 2009, ApJ, 694, 1517
Dannerbauer, H., Kurk, J. D., De Breuck, C., et al. 2014, A&A, 570, A55
Dey, A., Bian, C., Soifer, B. T., et al. 2005, ApJ, 629, 654
Dey, A., Lee, K.-S., Reddy, N., et al. 2016, ApJ, 823, 11
Dijkstra, M., & Loeb, A. 2009, MNRAS, 400, 1109
Erb, D. K., Bogosavljević, M., & Steidel, C. C. 2011, ApJL, 740, L31
Fardal, M. A., Katz, N., Gardner, J. P., et al. 2001, ApJ, 562, 605
Faucher-Giguère, C.-A., Kereš, D., Dijkstra, M., Hernquist, L., & Zaldarriaga, M. 2010, ApJ, 725, 633
Francis, P. J., Woodgate, B. E., Warren, S. J., et al. 1996, ApJ, 457, 490
Gao, L., White, S. D. M., Jenkins, A., Stoehr, F., & Springel, V. 2004, MNRAS, 355, 819
Gawiser, E., Francke, H., Lai, K., et al. 2007, ApJ, 671, 278
Geach, J. E., Alexander, D. M., Lehmer, B. D., et al. 2009, ApJ, 700, 1
Giocoli, C., Tormen, G., & van den Bosch, F. C. 2008, MNRAS, 386, 2135
Gladders, M. D., & Yee, H. K. C. 2000, AJ, 120, 2148
Gladders, M. D., & Yee, H. K. C. 2005, ApJS, 157, 1
Goerdt, T., Dekel, A., Sternberg, A., et al. 2010, MNRAS, 407, 613
Gronwall, C., Ciardullo, R., Hickey, T., et al. 2007, ApJ, 667, 79
Guaita, L., Gawiser, E., Padilla, N., et al. 2010, ApJ, 714, 255
Haiman, Z., & Rees, M. J. 2001, ApJ, 556, 87
Haiman, Z., Spaans, M., & Quataert, E. 2000, ApJL, 537, L5
Hatch, N. A., De Breuck, C., Galametz, A., et al. 2011a, MNRAS, 410, 1537
Hatch, N. A., Kurk, J. D., Pentericci, L., et al. 2011b, MNRAS, 415, 2993
Hayashi, M., Kodama, T., Tadaki, K.-I., Koyama, Y., & Tanaka, I. 2012, ApJ, 757, 15
Hayes, M., Scarlata, C., & Siana, B. 2011, Natur, 476, 304
Hogg, D. W. 2008, arXiv:0807.4820
Hogg, D. W., Cohen, J. G., Blandford, R., & Pahre, M. A. 1998, ApJ, 504, 622
Ivison, R. J., Smail, I., Le Borgne, J.-F., et al. 1998, MNRAS, 298, 583
Jiang, F., & van den Bosch, F. C. 2016, MNRAS, 458, 2848
Kollmeier, J. A., Zheng, Z., Davé, R., et al. 2010, ApJ, 708, 1048
Kurk, J. D., Röttgering, H. J. A., Pentericci, L., et al. 2000, A&A, 358, L1
Lanzetta, K. M., Wolfe, A. M., & Turnshek, D. A. 1995, ApJ, 440, 435
Laursen, P., & Sommer-Larsen, J. 2007, ApJL, 657, L69
Lee, K.-S., Dey, A., Hong, S., et al. 2014, ApJ, 796, 126
Lilly, S. J., Le Fevre, O., Hammer, F., & Crampton, D. 1996, ApJL, 460, L1
Madau, P., Pozzetti, L., & Dickinson, M. 1998, ApJ, 498, 106
Matsuda, Y., Yamada, T., & Hayashino, T. 2004, AstHe, 97, 628
Matsuda, Y., Yamada, T., Hayashino, T., et al. 2005, ApJL, 634, L125
Matsuda, Y., Yamada, T., Hayashino, T., et al. 2011, MNRAS, 410, L13
Mawatari, K., Yamada, T., Nakamura, Y., Hayashino, T., & Matsuda, Y. 2012, ApJ, 759, 133
Møller, P., & Warren, S. J. 1998, MNRAS, 299, 661
Monet, D. G., Levine, S. E., Canzian, B., et al. 2003, AJ, 125, 984
Mori, M., & Umemura, M. 2006, Natur, 440, 644
Mullis, C. R., Rosati, P., Lamer, G., et al. 2005, ApJL, 623, L85
Nilsson, K. K., Tapken, C., Møller, P., et al. 2009, A&A, 498, 13
Oke, J. B. 1974, ApJS, 27, 21

Orsi, A., Lacey, C. G., Baugh, C. M., & Infante, L. 2008, MNRAS, 391, 1589
Overzier, R. A. 2016, A&ARv, 24, 14
Overzier, R. A., Bouwens, R. J., Cross, N. J. G., et al. 2008, ApJ, 673, 143
Overzier, R. A., Miley, G. K., Bouwens, R. J., et al. 2006, ApJ, 637, 58
Overzier, R. A., Nesvadba, N. P. H., Dijkstra, M., et al. 2013, ApJ, 771, 89
Palunas, P., Teplitz, H. I., Francis, P. J., Williger, G. M., & Woodgate, B. E. 2004, ApJ, 602, 545
Parzen, E. 1962, Stochastic Processes (San Francisco, CA: Holden-Day)
Prescott, M. K. M., Dey, A., Brodwin, M., et al. 2012, ApJ, 752, 86
Prescott, M. K. M., Kashikawa, N., Dey, A., & Matsuda, Y. 2008, ApJL, 678, L77
Prescott, M. K. M., Martin, C. L., & Dey, A. 2015a, ApJ, 799, 62
Prescott, M. K. M., Momcheva, I., Brammer, G. B., Fynbo, J. P. U., & Møller, P. 2015b, ApJ, 802, 32
Press, W. H., & Schechter, P. 1974, ApJ, 187, 425
Rigby, E. E., Hatch, N. A., Röttgering, H. J. A., et al. 2014, MNRAS, 437, 1882
Rosati, P., Borgani, S., & Norman, C. 2002, ARA&A, 40, 539
Rosdahl, J., & Blaizot, J. 2012, MNRAS, 423, 344
Rosenblatt, M. 1956, Ann. Math. Statist., 27, 832
Saito, T., Matsuda, Y., Lacey, C. G., et al. 2015, MNRAS, 447, 3069
Saito, T., Shimasaku, K., Okamura, S., et al. 2006, ApJ, 648, 54
Springel, V., White, S. D. M., Jenkins, A., et al. 2005, Natur, 435, 629
Stanford, S. A., Romer, A. K., Sabirli, K., et al. 2006, ApJL, 646, L13
Steidel, C. C., Adelberger, K. L., Shapley, A. E., et al. 2000, ApJ, 532, 170
Steidel, C. C., Bogosavljević, M., Shapley, A. E., et al. 2011, ApJ, 736, 160
Taniguchi, Y., Ajiki, M., Nagao, T., et al. 2005, PASJ, 57, 165
Taniguchi, Y., & Shioya, Y. 2000, ApJL, 532, L13
Tody, D. 1986, Proc. SPIE, 627, 733
Trenti, M., & Stiavelli, M. 2008, ApJ, 676, 767
van Dokkum, P. G. 2001, PASP, 113, 1420
Venemans, B. P., Kurk, J. D., Miley, G. K., et al. 2002, ApJL, 569, L11
Venemans, B. P., Röttgering, H. J. A., Miley, G. K., et al. 2007, A&A, 461, 823
Wylezalek, D., Galametz, A., Stern, D., et al. 2013, ApJ, 769, 79
Yamada, T., Nakamura, Y., Matsuda, Y., et al. 2012, AJ, 143, 79
Yang, Y., Walter, F., Decarli, R., et al. 2014a, ApJ, 784, 171
Yang, Y., Zabludoff, A., Dave, R., et al. 2006, ApJ, 640, 539
Yang, Y., Zabludoff, A., Eisenstein, D., & Davé, R. 2010, ApJ, 719, 1654
Yang, Y., Zabludoff, A., Jahnke, K., et al. 2011, ApJ, 735, 87
Yang, Y., Zabludoff, A., Jahnke, K., & Davé, R. 2014b, ApJ, 793, 114
Yang, Y., Zabludoff, A. I., Zaritsky, D., & Mihos, J. C. 2009, ApJ, 702, 1683
Zeldovich, Y. B., Levich, E. V., & Syunyaev, R. A. 1972, ZhETF, 62, 1392
Zheng, Z., Cen, R., Weinberg, D., Trac, H., & Miralda-Escudé, J. 2011, ApJ, 739, 62